Sky cooling-driven radiant-capacitive hydronic system for all-day building cooling — Supplementary Material

Davide Forte[a], Eduardo González-Cruz[b], Lorenzo Pattelli[c], Claudio Belotti[d], Gloria Pérez[b], Pietro Asinari[a,c], Matteo Fasano[a]

[a]*Department of Energy, Politecnico di Torino, Corso Duca degli Abruzzi 24, Torino, 10129, Italy*
[b]*Eduardo Torroja Institute for Construction Science (IETCC), Spanish National Research Council (CSIC), Serrano Galvache 4, Madrid, 28033, Spain*
[c]*Istituto Nazionale di Ricerca Metrologica, Strada delle Cacce 91, Torino, 10135, Italy*
[d]*Istituto Nazionale di Ottica (CNR-INO), Via Madonna del Piano 10, Sesto Fiorentino, Firenze, 50019, Italy*

S1. Building: additional information

In this study, two distinct single-family residential buildings are simulated, representing reference cases for Spain and Italy. The buildings are located in Madrid and Rome, respectively. The overall heat transfer coefficients (htc) of the lumped elements of the buildings have been obtained from Tabula database [1], corresponding to the *Improved standard* category for constructions built after 2006 in both locations. The thermal capacities of the external building components have been calculated by integrating the stratigraphic information of the building envelopes—sourced from references [2] and [3] for Spain and Italy, respectively, with the thermal properties of conventional construction materials [4]. Conversely, the thermal capacities of the internal masses are consistent with the national building standards of Spain and Italy [5, 6]. The general thermal and optical characteristics of the lumped elements in the building models are presented in Table S1 for both locations.

Table S1: Building thermal and optical properties for Madrid and Rome (post-2006, improved standard)

Parameter	Symbol	Madrid	Rome	Ref.
Ext. walls global htc ($\mathrm{W\,m^{-2}\,K^{-1}}$)	$U_{\text{ext-e}}$	0.20	0.27	[2, 3]
Roof global htc ($\mathrm{W\,m^{-2}\,K^{-1}}$)	$U_{\text{ext-r}}$	0.48	0.22	[2, 3]
Floor global htc ($\mathrm{W\,m^{-2}\,K^{-1}}$)	$U_{\text{ext-f}}$	0.28	0.30	[2, 3]
Windows global htc ($\mathrm{W\,m^{-2}\,K^{-1}}$)	$U_{\text{ext-wi}}$	1.66	1.80	[2, 3]
Int. masses htc ($\mathrm{W\,m^{-2}\,K^{-1}}$)	U_{int}	3.72	3.72	assumed
Ext. walls heat cap. ($\mathrm{kJ\,m^{-2}\,K^{-1}}$)		376	351	[2, 3, 4]
Roof heat cap. ($\mathrm{kJ\,m^{-2}\,K^{-1}}$)		222	240	[2, 3, 4]
Floor heat cap. ($\mathrm{kJ\,m^{-2}\,K^{-1}}$)		574	665	[2, 3, 4]
Windows heat cap. ($\mathrm{kJ\,m^{-2}\,K^{-1}}$)		13	13	[2, 3, 4]
Int. masses heat cap. ($\mathrm{kJ\,m^{-2}\,K^{-1}}$)		80	80	[5, 6]
Windows g-factor	g_{wi}	0.67	0.67	[2, 3]
Ext. walls solar absorptivity	$\alpha_{\text{ext-wi}}$	0.60	0.60	assumed
Ext. walls thermal emissivity	$\varepsilon_{\text{ext-wi}}$	0.90	0.90	assumed
Roof solar absorptivity	$\alpha_{\text{ext-r}}$	0.35	0.35	assumed
Roof thermal emissivity	$\varepsilon_{\text{ext-r}}$	0.90	0.90	assumed

The buildings under consideration share identical geometric characteristics at both locations, comprising a reference floor area (A_{ref}) of $120\,\mathrm{m^2}$ distributed across two stories. Each building exhibits an aspect ratio of 1, with all four facades oriented toward the cardinal directions and a flat roof configuration. Table S2 presents the geometric specifications of the opaque external surfaces, while Table S3 provides the corresponding information for the window geometry.

Table S2: Geometrical parameters of the building, opaque surfaces

Parameter	Symbol	Value
Ext. walls area ($\mathrm{m^2}$)	$A_{\text{ext-e}}$	176.4
Roof area ($\mathrm{m^2}$)	$A_{\text{ext-r}}$	67.7
Floor area ($\mathrm{m^2}$)	$A_{\text{ext-f}}$	67.7
Story height (m)	z_{st}	3.0

Table S3: Geometrical parameters of the building, windows

Parameter	Symbol	Value
North window area ($\mathrm{m^2}$)	$A_{\text{ext.Nwi}}$	2.2
South window area ($\mathrm{m^2}$)	$A_{\text{ext.Swi}}$	2.2
West window area ($\mathrm{m^2}$)	$A_{\text{ext.Wwi}}$	8.3
East window area ($\mathrm{m^2}$)	$A_{\text{ext.Ewi}}$	7.2
Window height (m)	$z_{\text{v-wi}}$	1.5
Window length (m)	$z_{\text{h-wi}}$	1.25
Frame area ratio (%)	f_{wi}	30
Horizontal sunshade depth (m)	$z_{\text{vs-wi}}$	0.15
Vertical sunshade depth (m)	$z_{\text{hs-wi}}$	0.15

The thermal balance equation at the air mass inside the building, neglecting the latent effect of moisture is:

$$-Q_{\text{ext}} - Q_{\text{sol-o}} - Q_{\text{sol-t}} - Q_{\text{vent}} - Q_{\text{gen}} = -C_{\text{air}} \frac{\mathrm{d}T_{\text{b}}}{\mathrm{d}t} \tag{S1}$$

$C_{\text{air}} \frac{\mathrm{d}T_{\text{b}}}{\mathrm{d}t}$ is the variation of internal energy of the mass of air, where C_{air} ($\mathrm{J\,K^{-1}}$) is the thermal capacity of air.

Q_{ext} is the heat transmitted through external surfaces

$$Q_{\text{ext}} = A_{\text{ext}} U_{\text{ext}} (T_{\text{ext}} - T_{\text{b}}) \tag{S2}$$

where T_{b} is the average indoor temperature and T_{ext} is the external ambient temperature, equal to the temperature of air T_{air} for external walls, windows and roof, and to the temperature of the ground T_{gr} for the floor. A_{ext} is the surface of the external surface and U_{ext} its global heat transfer coefficient. For the i-th surface constituted by j plane layers of solid material and w

convective layers

$$U_{\text{ext},i} = \frac{1}{\sum_j \frac{s_{ij}}{k_{ij}} + \sum_w \frac{1}{h_{\text{c,air},iw}}} \tag{S3}$$

s_j and k_j are, respectively, the thickness and thermal conductivity of the j-th layer, $h_{\text{c,air},w}$ is the convective heat transfer coefficient of the w-th convective layer. Depending on the geometry of the surface exposed to the natural convection of air, a different value of $h_{\text{c,air},w}$ has been chosen, as reported in Ref. [4].

$Q_{\text{sol-o}}$ is the solar load absorbed by the external opaque surfaces (walls and roof):

$$Q_{\text{sol-o}} = \alpha_{\text{ext}} A_{\text{ext}} G \cos\theta_{\text{sol}} \tag{S4}$$

where α_{ext} is the external surface solar absorptivity, G is the global solar irradiance and θ_{sol} is the solar incidence angle. This last term was calculated using NREL Solar Position Algorithm [7], inputting as parameters the location (latitude, longitude and elevation), the surface tilt and orientation and the day of the year.

$Q_{\text{sol-t}}$ is the solar load transmitted by the external transparent surfaces (windows)

$$Q_{\text{sol-t}} = g_{\text{wi}} \xi_{\text{wi}} (1 - f_{\text{wi}}) A_{\text{ext-wi}} G \cos\theta_{\text{sol}} \tag{S5}$$

where f_{wi} is the percentage of the frame area with respect to total area of the window and g_{wi} is the window g-factor, assumed constant and independent of solar incidence angle. ξ_{wi} is the window sunlit area fraction, function of the location (latitude and longitude), the window tilt and orientation, the window geometry ($z_{\text{v-wi}}$, $z_{\text{h-wi}}$), the sun shadings geometry ($z_{\text{vs-wi}}$, $z_{\text{hs-wi}}$) and the day of the year. ξ_{wi} was calculated using the equations from Ref. [8]. Equations S4 and S5 assume that the diffuse component of global irradiance is isotropic.

The term Q_{vent} represents the heat exchange resulting from natural ventilation and infiltration, and is defined by the following expression:

$$Q_{\text{vent}} = \delta K_{\text{air}} (T_{\text{air}} - T_{\text{b}}), \tag{S6}$$

where δ denotes the air change rate, comprising both intentional natural ventilation and unintentional infiltration. The air change schedule is specified as follows: between 8:00 AM and 10:00 PM, δ is maintained at a low value of $0.3\,\text{h}^{-1}$ to minimize heat gains from the relatively high external air temperature. During the remaining hours, δ is increased to $1\,\text{h}^{-1}$ to enhance building cooling by utilizing the lower ambient nighttime temperatures.

The heat generation inside the building, related to the presence of people and electric devices, is simulated as a constant thermal load, always positive:

$$Q_{\text{gen}} = q_{\text{gen}} A_{\text{ref}}, \tag{S7}$$

where q_{gen} is the heat generated per unit surface, for which a value of $0.4\,\text{W m}^{-2}$ was considered [1].

The building is represented as a network of thermal resistances. Each internal and external surface comprises one to four layers of distinct materials, each defined by its specific heat capacity and thermal transmittance. Radiative heat exchange due to thermal re-radiation is considered only on the roof surface exposed to the sky, owing to the elevated temperatures it experiences, while it is neglected on all other surfaces. All lumped thermal masses, including humid air, are initialized at a temperature of 27 °C. The entire system is modeled within Simscape environment.

Eq. (S1) represents a passive building and does not account for its interaction with the hydronic cooling system. The updated thermal balance equation (Eq. S17), incorporating this interaction, is presented at the end of the next paragraph following the introduction of the radiant ceiling model.

S2. Radiant Capacity Modules: additional information

The Radiant Capacity Modules (RCMs) comprise galvanized steel parallelepiped enclosures filled with stationary water and installed in direct contact with the room ceiling. A copper coil is embedded within each module, conveying the chilled water supplied from the radiative panels. All RCMs are connected in parallel to a common inlet manifold, and their total number constitutes a design parameter varied in the simulations. The detailed geometry of each RCM is given in Table S4, while its thermal and optical properties in Table S5.

Table S4: Geometrical parameters of a RCM

Parameter	Symbol	Value
RCM bottom surface (m^2)	$A_{\text{RCM-bot}}$	0.81
RCM lateral surface (m^2)	$A_{\text{RCM-lat}}$	0.23
Water mass in RCM (kg)	m_{RCM}	52.65
Coil length (m)	$L_{\text{RCM-coil}}$	9.5
Coil diameter (m)	$d_{\text{RCM-coil}}$	0.95×10^{-2}
Coil inner roughness (m)		15×10^{-6}

Table S5: Thermal and optical properties of a RCM

Parameter	Material	Value
RCM box thermal conductivity ($\text{W m}^{-1}\,\text{K}^{-1}$)	steel	50
Coil thermal conductivity ($\text{W m}^{-1}\,\text{K}^{-1}$)	copper	390
RCM bottom surface thermal emissivity (–)	galvanized steel	0.3

The water contained within the RCM is modeled as a lumped thermal mass that exchanges heat with the top, bottom, and lateral steel plates, as well as with the internal copper coil. Due to the high thermal conductivity of both the steel enclosure and the copper coil, conductive resistances within these components are considered negligible. Furthermore, the thermal mass of the steel and copper elements is assumed to be negligible relative to that of the stored water. Consequently, the following thermal energy balance equation can be formulated for each RCM:

$$\begin{aligned} &- Q_{\text{conv-box}} + Q_{\text{conv-coil}} - Q_{\text{rad-wall}} - Q_{\text{rad-f}} \\ &- \sum_i Q_{\text{RCM-int},i} = -c_{\text{p,w}}\, m_{\text{RCM}}\, \frac{\text{d}T_{\text{RCM}}}{\text{d}t} \end{aligned} \tag{S8}$$

where $c_{p,w}$ is the specific heat of water and T_{RCM} is the water mass temperature.

$Q_{conv\text{-}box}$ is the term related to natural convection of air on the bottom surface of the RCM and can be expressed as:

$$Q_{conv\text{-}box} = A_{RCM\text{-}bot} h_{c,RCM\text{-}air} (T_b - T_{RCM}) \tag{S9}$$

where $h_{c,RCM\text{-}air}$ is the natural convective heat transfer coefficient for air on an horizontal ceiling. A value of $5.88\,W\,m^{-2}\,K^{-1}$ was considered [4].

The term $Q_{conv\text{-}coil}$ denotes the heat transfer between the copper coil and the water mass within the RCM enclosure, and is expressed as:

$$Q_{conv\text{-}coil} = A_{coil} h_{c,RCM\text{-}coil} \left(T_{RCM} - \bar{T}_{coil}\right) \tag{S10}$$

where A_{coil} is the external surface of the coil, $\bar{T}_{coil}$ represents the average temperature of the coil, and $h_{c,RCM\text{-}coil}$ is the convective heat transfer coefficient between the pipe surface and the surrounding water. This coefficient is determined using an empirical correlation for natural convection around a circular cylinder:

$$h_{c,RCM\text{-}coil} = Nu_{RCM\text{-}coil} \frac{k_w}{L_{RCM\text{-}coil}} \tag{S11}$$

Here, k_w is the thermal conductivity of water, and $Nu_{RCM\text{-}coil}$ is the Nusselt number, calculated according to the correlation reported in [9]:

$$Nu_{RCM\text{-}coil} = 0.48\,(Pr_w Gr_w)^{0.25} \tag{S12}$$

with Pr_w and Gr_w denoting the Prandtl and Grashof numbers for water, respectively. For the geometry considered, the Grashof number is given by:

$$Gr_w = 9.81 \beta_w \frac{d^3_{RCM\text{-}coil}}{\nu_w^2} \left(T_{RCM} - \bar{T}_{coil}\right) \tag{S13}$$

where β_w is the isobaric thermal expansion coefficient of water, and ν_w is its kinematic viscosity. Although the applied correlation is originally formulated for natural convection on vertical cylinders, the validation procedure demonstrated satisfactory accuracy in modeling convective heat transfer along the coil under analysis. The average coil temperature is computed using conventional correlations for flow in circular pipes, implemented within Simscape blocks. The RCM system is modeled using a hybrid approach, with the coil specifically characterized in Simscape.

The radiative fluxes $Q_{rad\text{-}wall}$ and $Q_{rad\text{-}f}$ represent the heat exchange by radiation between the RCM and the surrounding vertical walls, and between the RCM and the floor, respectively. In general, the bottom surface of each RCM radiatively exchanges heat with four vertical walls and the horizontal floor. Radiative contributions from the lateral surfaces of the RCMs are neglected, as these surfaces do not have a direct line of sight to the walls or the ground, except in the case of the lateral sides of the outermost RCMs in the array. The radiative heat exchanged between the i-th RCM and the s-th surface, with both modeled as broadband gray emitters, is expressed as:

$$Q_{rad,i} = \frac{\sigma F_{is}}{\frac{1}{\varepsilon_{RCM}} + \frac{1}{\varepsilon_{s,s}} - 1} A_{RCM\text{-}bot} \left(T^4_{s,s} - T^4_{RCM,i}\right) \tag{S14}$$

where σ is the Stefan–Boltzmann constant, F_{is} is the view factor between the RCM and the surface under consideration, T_s is the surface temperature, ε_{RCM} is the emissivity of the RCM, and ε_s is the emissivity of the surface (a value of 0.7 is adopted for both the walls and the floor). The view factor F_{is} varies depending on the spatial configuration of the RCM relative to the surrounding surfaces. Specifically, the equations used to compute the view factors between two horizontal surfaces of different size, and between a horizontal and a vertical surface of different size, are those provided in Ref. [10].

The term $\sum_i Q_{RCM\text{-}int,i}$ represents the thermal interaction between adjacent RCMs. Each RCM may be in contact with up to four neighboring modules. However, this term is assumed to be zero, as all RCMs are ideally maintained at the same temperature due to their parallel hydraulic connection.

The useful effect of the RCMs—namely, the heat removed from the indoor environment—can be quantified based on the change in enthalpy of the water flowing through the embedded coils. Neglecting the thermal inertia of the coil structure and the water contained within the coil, which is negligible compared to the stationary water volume inside the RCM, the thermal balance for a single coil can be expressed as:

$$Q_{conv\text{-}coil} = c_{p,w} \dot{m}_{w\text{-}RCM} \left(T_{w\text{-}RCM,out} - T_{w\text{-}RCM,in}\right) \tag{S15}$$

where $\dot{m}_{w\text{-}RCM}$ is the mass flow rate of water through each RCM, and $T_{w\text{-}RCM,out} - T_{w\text{-}RCM,in}$ represents the temperature rise of the water. The total useful energy removed by the entire array of RCMs is given by:

$$E_{RCM} = \sum_{i=1}^{n_{RCM}} \int_0^{t_{max}} Q_{conv\text{-}coil,i}(t)\,dt \tag{S16}$$

where n_{RCM} is the number of RCMs connected in parallel, and t_{max} is the total duration of the simulation.

The updated thermal balance equation of indoor air (Eq. (S1)) considering the cooling effect of RCMs is:

$$\begin{aligned} &- Q_{ext} - Q_{sol\text{-}o} - Q_{sol\text{-}t} - Q_{vent} - Q_{gen} \\ &+ \sum_i^{n_{RCM}} Q_{conv\text{-}box,i} = -C_{air} \frac{dT_b}{dt} \end{aligned} \tag{S17}$$

S3. Sky Radiators: additional information

The Sky Radiators (SRs) are modeled as flat-plate panels with the DRC material applied to the sky-facing surface. Each panel comprises a polypropylene slab containing several parallel circular channels and a thick polystyrene insulation layer on the bottom. The physical presence of the DRC film is neglected due to its low thickness (~200 µm); only its spectral properties are assigned to the sky-facing surface. Detailed geometric parameters are provided in Table S6, and thermal properties in Table S7.

Modeling the geometry of the DRC panel in full detail would require simulating fluid flow through 208 parallel channels and accounting for thermal interactions among them. However,

Table S6: Geometrical parameters of a SR

Parameter	Symbol	Value
Sky-facing surface (m^2)	A_p	2.27
Panel length (m)	L_{SR}	1.89
Panel width (m)		1.20
Number of parallel channels (–)		208
Channel diameter (m)	$D_{pipe\text{-}SR}$	4.3×10^{-3}
Channel spacing (m)		0.6×10^{-3}
Plate thickness (m)		5.5×10^{-3}
Insulation thickness (m)		40×10^{-3}

Table S7: Thermal properties of a SR

Parameter	Material	Value
Plate th. conductivity ($W\,m^{-1}\,K^{-1}$)	polypropylene	0.15
Back insulation ($W\,m^{-1}\,K^{-1}$)	extruded polystyrene	0.035
Sky-facing surface emissivity (–)	DRC material	see main text

since all channels are arranged in parallel and all SRs are likewise connected in parallel, and given that lateral heat transfer across the panel surfaces is neglected, the temperature drop along each channel is assumed to be identical. Consequently, the simulation domain is reduced to a single representative channel, which adequately captures the thermal and hydraulic behavior of the entire panel. Despite the simplifications involved, the sky radiator model was successfully validated, as discussed in the Main Text, Section 3.1.

The panel is modeled as a thermal resistance network comprising the thermal resistances of the polypropylene plate, the polystyrene insulation, and those arising from laminar water flow within the channels. These heat transfer mechanisms are implemented in the Simscape environment using standard thermal and fluid domain components available in the software. To improve accuracy in resolving temperature gradients along the flow direction, the model domain is discretized into ten segments along the panel length.

For clarity, the terms $Q_{non\text{-}rad}$ and Q_{net} from the panel thermal balance equation (Eq. 1) are computed within Simscape using its conventional blocks. In contrast, the radiative terms Q_p, Q_{sol}, and Q_{atm} are spectrally dependent and cannot be computed directly in Simscape. Therefore, Q_{sol} and Q_{atm} are precomputed across the full simulation time domain prior to the dynamic simulation. The panel radiative emission term Q_p is evaluated dynamically via a one-dimensional lookup table that relates panel temperature, calculated during simulation, to the corresponding radiative power output. The sum of these radiative fluxes is then applied in Simscape as boundary heat flux input on the sky-facing surface. Further methodological details are available in a previous study [11].

S4. Water distribution network: additional information

The water distribution circuit comprises the piping network connecting the SRs to the radiative RCMs, a buffer tank, and a circulation pump.

The buffer tank is an insulated cylindrical reservoir designed to dampen pressure fluctuations within the circuit. The connecting pipes are insulated cylindrical conduits made of multilayer polyethylene of raised temperature resistance (PERT) reinforced with an intermediate aluminum layer (PERT-AL-PERT). Their lengths were estimated based on geometric considerations of the physical layout, while their thermal insulation performance was derived from experimental data obtained from the validation setup. This data enabled estimation of the average temperature drop per meter of pipe length ($°C\,m^{-1}$). The design working pressure of the system is 1.2 bar.

Both the buffer tank and the piping system are modeled in the Simscape environment using standard hydraulic and thermal components. These components allow for the computation of thermal interactions with the surrounding environment as well as pressure losses due to fluid friction. The geometrical and thermal parameters used in the simulations are summarized in Tables S8 and S9, respectively.

Table S8: Geometrical parameters of the water distribution network

Parameter	Symbol	Value
Pipe length, SRs outlet to RCMs inlet (m)	L_{pipe1}	20
Pipe length, RCMs outlet to tank inlet (m)	L_{pipe2}	15
Pipe length, tank outlet to SRs inlet (m)	L_{pipe3}	5
Buffer tank volume (m^3)		0.45
Buffer tank cross-sectional area (m^2)		0.54

Table S9: Thermal parameters of the water distribution network

Parameter	Value
Pipe thermal losses ($°C\,m^{-1}$)	0.0238
Buffer tank global htc ($W\,m^{-2}\,K^{-1}$)	1

The circulation pump is modeled as an isothermal flow-rate source. Its power consumption, Q_{pump}, is calculated as:

$$Q_{pump} = \frac{\dot{V}\Delta p_{tot}}{\eta_{pump}} \tag{S18}$$

where $\dot{V}$ is the volumetric water flow rate, η_{pump} is the pump electromechanical efficiency (assumed to be 67.5 %), and Δp_{tot} represents the total pressure drop in the circuit. This includes distributed pressure losses in the SRs, RCM coils, and connecting conduits, as well as localized losses at the inlet and outlet manifolds of the SRs and RCMs, and within the buffer tank.

Distributed pressure drops are computed as:

$$\Delta p_{dis} = f_D \frac{L}{D} \frac{\rho_w v_w^2}{2} \tag{S19}$$

where L is the pipe length, D the pipe diameter, ρ_w the water density, v_w the water velocity, and f_D the Darcy friction factor, equal to $64/Re$ in laminar flow and computed via the Swamee-Jain correlation in turbulent flow [12]. This formulation is applied to pressure losses in the SR and connecting pipes. For RCM coils, curvature effects are accounted for using White's correlation for curved pipes [13].

Localized pressure drops are computed as:

$$\Delta p_{loc} = k_{loc} \frac{\rho_w v_w^2}{2} \tag{S20}$$

where k_{loc} is a factor depending on the geometry of the system generating the concentrated pressure losses. Table S10 summarizes the different sources of localized pressure losses and the correlations used to determine k_{loc}.

Table S10: Values of k_{loc} used in the estimation of localized pressure losses

Device	Details	Information
SR	manifold inlet	$k_{loc} = 1$
SR	splitting	Ref. [14]
SR	merging	Ref. [14], norm. curv. radius of 0.188
SR	manifold outlet	$k_{loc} = 0.5$
RCM	splitting	Ref. [14]
RCM	merging	Ref. [14], norm. curv. radius of 0.188
tank	inlet	$k_{loc} = 1$
tank	outlet	$k_{loc} = 0.5$

The calculated pressure losses in the hydraulic circuit represent a first-order approximation, given the complexity of the circuit geometry. Specifically, the effects of pipe bends and vertical segments, associated with changes in gravitational potential energy, were not explicitly modeled. To account for these unmodeled contributions and to maintain a conservative estimation, the measured pressure drop values were increased by 20 %.

S5. Model Validation: additional information

The numerical model is validated using experimental data from a full-scale demonstrator located in Arganda del Rey (Madrid, Spain). The demonstrator includes a small building, ceiling-mounted RCMs, SRs, a thermal storage tank, a water distribution system, and sensorized material samples. A comprehensive description of the setup, as well as the measurement and data acquisition systems, is provided in Ref. [15]. Here, only a general overview of the setup is presented, along with its key characteristics, to ensure replicability in the modeling process.

The RCMs are connected in parallel and are identical to those employed in the large-scale residential building, as detailed in Section S2. Similarly, the parallel-connected SRs, located outside the building, share the same specifications as those described in Section S3 for the large-scale system.

The material samples are 20 cm × 20 cm specimens, framed and backed with extruded polystyrene insulation. These samples are used to monitor the temperatures of the different materials under fully passive conditions, without underlying water flow as in the SRs. While the experimental setup includes various materials, validation focuses just on two samples: one made of polypropylene and another consisting of polypropylene coated with the DRC material.

The water distribution system comprises a circulation pump, two storage tanks (with capacities of 50 L and 1000 L), and connecting pipelines. The insulation of the pipelines matches the specifications provided in Section S4. Pipe lengths are as follows: 18.6 m between the SR outlet and the RCM inlet, 12.2 m from the RCM outlet to the tank, and 5.2 m from the tank to the SR inlet.

The building, oriented 11° southeast, consists of three rooms: a central lobby (1.47 m × 5.79 m × 2.92 m) and two identical side rooms (5.61 m × 2.68 m × 2.92 m each) with a volume of 44 m^3 each. The room equipped with RCMs is referred to as the experimental cell (EC), while the unconditioned room is designated as the control cell (CC). Both rooms are equipped with southeast-facing windows. The detailed stratigraphy of the building is provided in Table S11, and window specifications are reported in Table S12. Given the high insulation level of the building, solar irradiance transmitted through the windows constitutes the dominant thermal gain. Therefore, accurate modeling of the windows and the shading effects on them is essential. The demonstrator is elevated above the ground, therefore air convection takes place below the floor surface.

The model validation is conducted on two experimental series, referred to as Series 1 and Series 2. Table S13 summarizes the setup characteristics and key information for each series. For detailed meteorological data and experimental results, the reader is referred to the reference publication [15].

The model validation is carried out by first assessing each subsystem independently (the EC, the CC and the SRs), followed by validation of the complete integrated system. The results presented in the main text focus on the isolated validation of each subsystem, where only the component under analysis is dynamically simulated, while the others are treated as boundary conditions. For example, when validating the EC, the CC is not simulated; instead, its temperature, experimentally measured, is imposed as a boundary condition at the internal wall shared with the EC. Likewise, the SRs are not modeled, and the measured inlet temperature to the RCMs is used as input. In addition to the individual validations, the full system is also simulated and compared against experimental data. The integrated model demonstrates strong agreement with measurements, confirming the validity of the modeling approach across both component-level and system-level scales.

Although each experimental series lasts five days, only the final four days are used for model validation. The first day is excluded due to greater discrepancies between simulations and measurements, primarily caused by unknown initial conditions. This issue is particularly significant for the CC model: owing to the high thermal insulation of the room, even small errors in the initial temperature can lead to notable deviations. Only the initial air temperature is known from the experiments, while the temperatures of the wall, floor, roof, and window layers remain unknown. To address this, a brute-force algorithm is employed to identify the optimal set of initial temperatures for the internal components of the CC. The algorithm evaluates all feasible combinations by simulating the thermal behavior of the CC over the meteorological series and selects the one minimizing the Mean Absolute Percentage Error (MAPE). The initial temperatures of each component must remain within physically valid ranges. After a brief initial mismatch, the model aligns well with experimental data for the remaining days.

The EC model is less sensitive to uncertainties in initial conditions due to the significant thermal inertia of the water in the

Table S11: Arganda del Rey demonstrator stratigraphy of external walls, internal walls, roof and ceiling. Thermal zones: experimental cell (EC), control cell (CC), lobby (L). Cardinal orientation: north (N), south (S), west (W), east (E). Physical quantities: convective heat transfer coefficient (h_c), thermal conductivity (λ), thickness (t), global heat transfer coefficient (U). Layers: ext = external air layer, int = internal air layer, gap = wall air gap, 1 = wooden shading (layer 1), 2 = layer 2, 3 = layer 3, 4 = layer 4.

Zone	**Area** m^2	$h_{c,ext}$ $W\,m^{-2}\,K^{-1}$	λ_1 $W\,m^{-1}\,K^{-1}$	t_1 cm	$h_{c,gap}$ $W\,m^{-2}\,K^{-1}$	λ_2 $W\,m^{-1}\,K^{-1}$	t_2 cm	λ_3 $W\,m^{-1}\,K^{-1}$	t_3 cm	λ_4 $W\,m^{-1}\,K^{-1}$	t_4 cm	$h_{c,in}$ $W\,m^{-2}\,K^{-1}$	U $W\,m^{-2}\,K^{-1}$
EC W / CC E	19.1	25.00	0.130	2.5	5.50	0.130	1.8	0.034	60	0.130	1.8	7.69	0.054
EC S / CC S	6.6	25.00	0.130	2.5	5.50	0.130	1.8	0.034	60	0.130	1.8	7.69	0.054
L W / E	6.8	25.00	0.130	2.5	5.50	0.130	1.8	0.034	60	0.130	1.8	7.69	0.054
L N	17.0	25.00	0.130	2.5	5.50	0.130	1.8	0.034	60	0.130	1.8	7.69	0.054
EC–CC	16.6	7.69	-	-	-	0.130	1.8	0.034	40	0.130	1.8	7.69	0.081
L–EC/CC	8.5	7.69	-	-	-	0.130	1.8	0.034	40	0.130	1.8	7.69	0.081
Roof	39.2	25.00	-	-	-	0.130	1.8	0.034	60	0.130	1.8	5.88	0.055
Floor	39.2	25.00	-	-	-	0.130	1.8	0.034	60	0.130	1.8	5.88	0.055

Table S12: Geometrical, thermal and optical parameters of the window of Arganda del Rey demonstrator.

Parameter	**Value**
Window total area (m^2)	1.87
Glass area (m^2)	1.36
Global htc ($W\,m^{-2}\,K^{-1}$)	0.59
Window g-factor	0.58
Window length (m)	1.50
Window width (m)	1.25
Window vertical overhang (m)	0.30
Window horizontal overhang (m)	0.30

Table S13: Operational parameters of Series 1 and Series 2

Parameter	**Series 1**	**Series 2**
Date	20/08–24/08/2024	8/08–12/08/2024
Operating hours	10:00 PM–8:00 AM	10:00 PM–8:00 AM
Material of the SRs emitter	SpaceCool Film_Silver	Black polypropylene
Number of RCMs	8	8
Number of SRs	5	5
Flow rate ($L\,h^{-1}$)	363	387
Tank size (L)	50	1000

ceiling RCMs. The SRs model is only marginally affected by initial conditions because of their low thermal inertia.

The error metrics used during the validation process are the MAPE, the Root Mean Square Error (RMSE), and the Index Of Agreement (IOA). Let x be the experimental value and x_m the value obtained from the model. The three aforementioned metrics are defined as follows:

$$\mathrm{MAPE} = \frac{100}{n}\sum_{i=1}^{n}\left|\frac{x_i - x_{m,i}}{x_i}\right| \tag{S21}$$

$$\mathrm{RMSE} = \sqrt{\frac{1}{n}\sum_{i=1}^{n}(x_i - x_{m,i})^2} \tag{S22}$$

$$\mathrm{IOA} = 1 - \frac{\sum_{i=1}^{n}(x_i - x_{m,i})^2}{\sum_{i=1}^{n}\left(\left|x_{m,i} - \bar{x}\right| + \left|x_i - \bar{x}\right|\right)^2} \tag{S23}$$

where n is the total number of values and $\bar{x}$ is the mean of the experimental values.

Table S14 presents the full results of the model validation on the demonstrator, using data from experimental Series 1 and 2.

Table S14: Results of model validation on Series 1 and Series 2

	Series 1			**Series 2**		
	MAPE (%)	RMSE	IOA (-)	MAPE (%)	RMSE	IOA (-)
T_{CC} (°C)	0.67	0.3	0.94	0.64	0.3	0.90
T_{EC} (°C)	0.70	0.2	0.98	0.86	0.3	0.96
T_{RCM} (°C)	1.52	0.4	0.97	1.49	0.5	0.97
T_{sample} (°C)	5.58	1.4	0.99	2.75	0.9	1.00
q_{net} ($W\,m^{-2}$)	-	11.1	0.97	-	12.3	0.95

An additional validation of the material model is presented in Figures 2d–e of the main text. Here, experimental data from the passive material samples are compared with the numerical model defined by Eq. 1. In this case, the system is solved under steady-state conditions, with the transient term set to zero and $q_{net} = 0\,W\,m^{-2}$, as there is no water flow. This assumption is justified by the low thermal inertia of the small square samples. Solving the steady-state equation allows to express the emitter temperature T_p as a function of varying irradiance G. The model output is presented as an area to account for the variability in relative humidity (RH), and results are parameterized with respect to ambient temperature T_{amb}. Model predictions are compared against experimental data including uncertainty: 5 % for irradiance and ±0.15 °C for temperature. Once defined the target ambient temperature for the parameterization T^*_{amb}, only the experimental data meeting the following criteria are chosen: $|T_{amb} - T^*_{amb}| \leq 0.5\,°C$, $20\,\% \leq RH \leq 40\,\%$ and $0.5\,m\,s^{-1} \leq u \leq 1.5\,m\,s^{-1}$, where u is the wind velocity. Also, only daytime data are selected, according to the constraint $G \geq 50\,W\,m^{-2}$.

The validation uses data from Series 1 and 2, along with an additional series conducted between 16/08–20/08/2024, as detailed in the reference publication. For the DRC material, the best agreement occurs at $T^*_{amb} = 30\,°C$, with a MAPE of 2.74 % and RMSE of 0.75 °C. The highest errors, MAPE = 4.09 % and RMSE = 1.71 °C, are observed at $T^*_{amb} = 40\,°C$. For the black polypropylene emitter, the minimum MAPE and RMSE are 2.27 % and 1.13 °C, respectively, at $T^*_{amb} = 30\,°C$, while the maximum values, 4.81 % and 2.62 °C, occur at $T^*_{amb} = 35\,°C$.

As a final remark, during the validation process, the radiative power absorbed by the SR from the atmosphere Q_{atm} is calculated in a different way compared to the procedure adopted for the simulations over the entire cooling season. Specifically, this approach is based on the model proposed in Ref. [16], which expresses the spectral atmospheric emissivity via a polynomial formulation:

$$\varepsilon_{\mathrm{atm}}(\lambda) = 1 - \exp\left[a_0(\lambda) + a_1(\lambda)y + a_2(\lambda)y^2 + a_3(\lambda)y^3\right] \quad \text{(S24)}$$

where y is the precipitable water vapor amount and a_0, a_1, a_2 and a_3 are fitting coefficients. The precipitable water vapor was estimated using a simple correlation from Ref. [17] that allows to express it as a function of air temperature and relative humidity.

Upon determining the spectral atmospheric emissivity, the radiative power absorbed from the atmosphere is calculated as follows:

$$Q_{\mathrm{atm}} = \pi A_{\mathrm{p}} \int_0^{\infty} \int_0^{\frac{\pi}{2}} \varepsilon_{\mathrm{p}}(\lambda,\theta)\varepsilon_{\mathrm{atm}}(\lambda) I_{\mathrm{b}}(\lambda, T_{\mathrm{amb}}) \sin(2\theta)\, \mathrm{d}\theta\, \mathrm{d}\lambda \quad \text{(S25)}$$

where A_{p} is the sky-facing surface, $\varepsilon_{\mathrm{p}}(\lambda,\theta)$ is the spectral-dependent and angular-dependent emissivity of the SR, and $I_{\mathrm{b}}(\lambda, T_{\mathrm{amb}})$ is the blackbody spectral radiance of the atmosphere evaluated at the ambient temperature.

During model validation, this formulation of Q_{atm} was adopted instead of that derived from the RRTM_LW model primarily for two reasons: (i) it is significantly less computationally demanding, and (ii) it relies exclusively on meteorological data (ambient temperature and relative humidity) directly measured at the experimental site, thus eliminating dependence on ERA5 reanalysis data, which are characterized by coarser spatial resolution and may be less representative of the local environmental conditions. It is important to note that this model is only applicable under clear-sky conditions, as it does not account for the impact of cloud cover on the atmospheric window. Consequently, the experimental data used for validation (Series 1 and 2) correspond to days with predominantly clear skies and minimal cloud presence.

S6. Building temperature setpoint definition

According to ASHRAE-55 standard, the comfort zone in buildings without mechanical ventilation [18] can be defined as (with an acceptability at 90 %):

$$T^*_{\mathrm{max}} = 0.31T_{\mathrm{rm}} + 20.3, \qquad T^*_{\mathrm{min}} = 0.31T_{\mathrm{rm}} + 15.3 \quad \text{(S26)}$$

where T^*_{max} and T^*_{min} are the extremis of the comfort range and T_{rm} is the outdoor running mean temperature. One valid approach for estimating T_{rm} is to use the monthly average outdoor temperature.

Based on Typical Meteorological Year (TMY) data, August is the hottest month in both Madrid and Rome, with mean outdoor temperatures of 27.28 °C and 26.77 °C, respectively. This results in comfort ranges of 28.8–23.8 °C for Madrid and 28.6–23.6 °C for Rome. However, as discussed in the main text, a conservative upper comfort limit of $T^*_{\mathrm{max}} = 27$ °C is adopted for both locations.

S7. Condensation index definition

To quantify the impact of condensation on both SRs and RCMs, a metric called condensation indicator (J) is introduced. This indicator represents the fraction of total simulation time during which the average temperature of the surface under analysis falls below the ambient dew point temperature (T_{dp}). The dew point temperature data used in the simulations are extracted from the ERA5 reanalysis database. For the indoor environment, the same dew point temperature as the outdoor environment is assumed. This assumption is considered reasonable given the passive ventilation strategy adopted for the building and the absence of any active systems regulating indoor humidity. The condensation indicator is defined through binary indicator functions for the RCMs, $\psi_{\mathrm{RCM}}(t)$, and the SRs, $\psi_{\mathrm{SR}}(t)$, as follows:

$$\psi_{\mathrm{RCM}}(t) = \begin{cases} 1, & \text{if } T_{\mathrm{RCM}}(t) \le T_{\mathrm{dp}}(t) \\ 0, & \text{otherwise} \end{cases} \quad \text{(S27)}$$

$$\psi_{\mathrm{SR}}(t) = \begin{cases} 1, & \text{if } T_{\mathrm{p}}(t) \le T_{\mathrm{dp}}(t) \\ 0, & \text{otherwise} \end{cases} \quad \text{(S28)}$$

Using these functions, the condensation indicators for RCMs and SRs are computed as:

$$J_{\mathrm{RCM}} = \frac{1}{t_{\mathrm{tot}}} \int_0^{t_{\mathrm{tot}}} \psi_{\mathrm{RCM}}(t)\, \mathrm{d}t \quad \text{(S29)}$$

$$J_{\mathrm{SR}} = \frac{1}{t_{\mathrm{tot}}} \int_0^{t_{\mathrm{tot}}} \psi_{\mathrm{SR}}(t)\, \mathrm{d}t \quad \text{(S30)}$$

where t_{tot} denotes the total simulation time. These indicators provide a time-averaged measure of condensation risk, offering a clear quantitative basis for assessing the susceptibility of DRC systems to moisture accumulation under varying climatic conditions.

S8. Effect of sky view factor

This paragraph addresses the modification of the thermal balance equation on the SRs when they are deployed in environments where obstacles partially obstruct the view of the sky. Urban obstacles, such as buildings, trees, or chimneys, act as infrared-emitting bodies, radiating thermal energy toward the SRs. At the same time, however, they may have a beneficial effect by providing shading, thereby reducing the amount of solar radiation absorbed. The "access" of the SRs to the sky can be quantified via a parameter called sky view factor (SVF), representing the fraction of the overlying hemispherical sky dome that is unobstructed by surrounding obstacles.

The purpose of this paragraph is not to reproduce the full complexity of a real urban environment with irregular obstacles, but rather to provide a simplified quantification of the general influence of the SVF on the performance of the DRC emitter. To this end, strong assumptions are adopted by representing the surroundings as an urban canyon, fully described by only two parameters: the obstacle height (H) and the distance between

obstacles (W). Under this assumption, the 2D sky view factor can be expressed as [19]:

$$\mathrm{SVF} = \cos\left[\arctan\left(\frac{H}{0.5W}\right)\right] = \cos\beta_{\mathrm{obs}} \tag{S31}$$

where β_{obs} is the angle from the center point of the observer to the maximum obstacle height. Considering that sidewalks and lanes have typically a width of 3 m and 4 m, respectively [19], the canyon width can be estimated as $W = 14$ m.

The SVF can now be incorporated into the thermal balance of the SRs (Eq. 1 in the main text), leading to a modified form [20], which becomes:

$$Q_{\mathrm{p}} - Q^{*}_{\mathrm{sol}} - Q^{*}_{\mathrm{atm}} - Q^{*}_{\mathrm{obs}} - Q_{\text{non-rad}} - Q_{\mathrm{net}} = -C_{\mathrm{p}}\frac{\mathrm{d}T_{\mathrm{p}}}{\mathrm{d}t}. \tag{S32}$$

The power absorbed from the atmosphere is modified under the assumption that the SRs emit and absorb uniformly over the entire solid angle–an approximation that is reasonably accurate for the DRC material employed in this study [21]–and that they "see" only a fraction of the sky equal to the SVF:

$$Q^{*}_{\mathrm{atm}} = \mathrm{SVF}\ Q_{\mathrm{atm}} \tag{S33}$$

The power absorbed from the surrounding obstacles is modeled by treating them as gray bodies (with an emissivity $\varepsilon_{obs} = 0.95$) emitting at a temperature T_{obs}:

$$Q_{\mathrm{obs}} = \pi A_{\mathrm{p}} \int_0^{\infty}\int_0^{\frac{\pi}{2}} \varepsilon_{\mathrm{obs}}\varepsilon_{\mathrm{p}}(\lambda,\theta)\ I_{\mathrm{b}}\left(\lambda, T_{\mathrm{obs}}\right)\sin\left(2\theta\right) d\theta d\lambda \tag{S34}$$

Then, this term is corrected using the SVF:

$$Q^{*}_{\mathrm{obs}} = (1 - \mathrm{SVF})\ Q_{\mathrm{obs}} \tag{S35}$$

Considering that the setup mainly works at nighttime and in low irradiance conditions, as a first approximation, T_{obs} was assumed equal to T_{amb}.

The power absorbed from solar radiation is adjusted to account for shading effects. In general, when the solar elevation angle is lower than the obstacle angle, β_{obs}, no direct solar radiation reaches the SRs; only diffuse radiation contributes. Accordingly, the solar irradiance incident on the SRs can be expressed as:

$$G^{*} = \begin{cases} G, & \text{if } \theta_{\mathrm{elev}} \geq \beta_{\mathrm{obs}} \\ G_{\mathrm{diff}}, & \text{if } \theta_{\mathrm{elev}} < \beta_{\mathrm{obs}} \end{cases} \tag{S36}$$

where θ_{elev} is the solar elevation angle (calculated with NREL solar position algorithm [7]) and G_{diff} is the diffuse solar irradiance. The decomposition between direct and diffuse solar radiation can be performed using Erbs' model [22]:

$$\frac{G_{\mathrm{diff}}}{G} = \begin{cases} 1 - 0.09K_{\mathrm{t}}, & K_{\mathrm{t}} \leq 0.22 \\ 0.9511 - 0.1604K_{\mathrm{t}} + 4.388K_{\mathrm{t}}^{2} & 0.22 < K_{\mathrm{t}} \leq 0.8 \\ \quad -16.638K_{\mathrm{t}}^{3} + 12.336K_{\mathrm{t}}^{4}, & \\ 0.165, & K_{\mathrm{t}} > 0.8 \end{cases} \tag{S37}$$

where K_{t} is the clearness index. The modified term accounting for solar irradiance absorption (corresponding to the modification of Eq. 4 in the main text) is:

$$Q_{\mathrm{sol}} = A_{\mathrm{p}}G^{*}\frac{\int_0^{\infty}\varepsilon_{\mathrm{p}}(\lambda)I_{\mathrm{AM1.5}}(\lambda)\,\mathrm{d}\lambda}{\int_0^{\infty}I_{\mathrm{AM1.5}}(\lambda)\,\mathrm{d}\lambda} \tag{S38}$$

After developing this framework, a case study was conducted for a building in Madrid under August TMY conditions, considering varying values of the SVF. To isolate the effect of the SVF, the building thermal load was assumed constant (a conservative assumption that neglects shading effects of obstacles on the building envelope and transparent surfaces). The results of this analysis are presented in Figure S7a.

S9. Effect of natural aging

Environmental aging of DRC materials is primarily driven by UV radiation, thermal aging, and chemical corrosion, with UV-induced degradation being the most critical for durability [23]. Some studies on natural aging of roof coatings show that longwave emissivity remains largely unchanged, whereas shortwave reflectivity can decrease significantly, compromising the cooling capability of the material [24]. These effects can be approximated in simulation models by adjusting the solar reflectivity of the DRC material, while assuming infrared emissivity remains constant.

A sensitivity analysis was performed to evaluate the effect of solar reflectivity reduction, considering decreases in the range of 1–10%. The analysis was conducted for a building in Madrid under August TMY conditions, representing the most critical period. The results, shown in Figure S7b, indicate that the system is largely unaffected by reductions in solar reflectivity. This behavior is explained by the fact that the DRC-based hydronic setup primarily operates during nighttime conditions, while daytime operation occurs only during periods of low to moderate solar irradiance.

S10. Effect of climate zone

The DRC-based hydronic system was designed and sized to achieve high levels of comfort in Madrid and Rome, both of which are characterized by temperate climates. The analysis is here extended to additional climate zones to assess how varying climatic conditions affect the system performance throughout the hot season. Four additional locations—Paris (France), Denver (USA), Las Vegas (USA), and Singapore—are investigated. TMY data for these locations were obtained from ERA5. Table S15 summarizes the information for each location, including their climatic zone classification according to the Köppen–Geiger (KG) system.

To isolate the effect of climate, the same DRC-based hydronic system and building model were adopted across all locations. For the hydronic system, a SR surface covering the entire roof was considered in order to fully exploit the available area.

Table S15: Geographical and climate data for selected locations

City	Latitude	Longitude	Altitude (m)	KG zone
Madrid (Spain)	40.417	−3.704	600	Csa/Bsh
Rome (Italy)	41.903	12.496	100	Csa
Paris (France)	48.857	2.352	50	Cfb
Denver (USA)	39.739	−104.985	1600	BSk
Las Vegas (USA)	36.170	−115.140	650	BWh
Singapore	1.290	103.852	0	Af

The number of RCMs was fixed at 70, a configuration that ensured high comfort levels in both Madrid and Rome. The configuration with high pipe insulation, as described in Section 4 of the main text, was employed.

For the sake of comparability, the same building typology and thermal characteristics were maintained across all locations. The reference building corresponds to a modern standard-insulated, two-story single-family house, with geometric features identical to those used for the Madrid and Rome cases (Table S2) and insulation characteristics reported in Table S16.

Table S16: Thermal and optical properties of the building used for location analysis.

Parameter	Madrid
Ext. walls global htc ($W\,m^{-2}\,K^{-1}$)	0.20
Roof global htc ($W\,m^{-2}\,K^{-1}$)	0.20
Floor global htc ($W\,m^{-2}\,K^{-1}$)	0.30
Windows global htc ($W\,m^{-2}\,K^{-1}$)	1.50
Int. masses htc ($W\,m^{-2}\,K^{-1}$)	3.72
Windows g-factor	0.60
Ext. walls solar absorptivity	0.60
Ext. walls thermal emissivity	0.90
Roof solar absorptivity	0.35
Roof thermal emissivity	0.90

With regard to the comfort zone, the same criterion was applied across all systems to ensure comparability. The maximum acceptable indoor temperature was set to 27 °C, while the hydronic system was switched off whenever the indoor temperature dropped below 19 °C to avoid overcooling. Since the locations are situated at different latitudes, the number of daylight hours varies significantly throughout the year. Consequently, a fixed-hour on/off control strategy could not be applied, and an alternative strategy was required. The rationale behind the new control approach is to keep the DRC-based system active whenever feasible, while preventing the SRs from transferring heat to the RCMs even under adverse meteorological conditions for radiative cooling. The circulation pump is activated whenever the difference between the average temperatures of RCMs (T_{RCM}) and SRs (T_p) exceeds 0.5°C: $T_{RCM} - T_P \geq 0.5\,°C$. This strategy demonstrated effective operation without the occurrence of unstable control behaviors such as chattering (rapid, repeated on/off switching around the setpoint).

The results of the location-based analysis are reported in Figure 8 of the main text.

S11. Economic and environmental analysis

A simple economic analysis is conducted for two case studies to provide preliminary insights into the economic viability of the DRC-based cooling systems. The case studies analyzed refer to the results of the location analysis performed in Section 4 of the Main text (results in Figure 8), focusing on the cities of Madrid and Rome. These locations were selected because, under their respective meteorological conditions, a fully DRC-based system was shown to satisfy the cooling demand while maintaining high comfort levels (CI above 99 % in both locations). The DRC-based cooling system adopted in the analysis comprises 29 SRs (ensuring a full roof coverage) and 70 RCMs. The results are summarized in Table S18.

The economic analysis compares the DRC-based system with a widely-adopted cooling system in European single-family buildings, consisting of multiple ductless air-to-air heat pumps. Considering the size of the single-family building and its thermal loads, three ductless heat pumps with a nominal evaporator capacity of $2.6\,kWh_{th}$ (standard size of $9000\,BTU\,h^{-1}$) were selected for both locations. The heat pump operates under a conventional single-stage vapor-compression refrigeration cycle (composed of evaporation, compression, condensation, and valve lamination) using R134a as refrigerant. Its thermodynamic characteristics are provided in Table S17.

Table S17: Thermodynamic states of the refrigeration cycle

State point	Pressure (bar)	Enthalpy ($kJ\,kg^{-1}$)	Quality (-)
Evaporator outlet	4.15	256.2	1
Compressor inlet	13.19	219	1
Compressor outlet	13.19	123.5	0
Evaporator inlet	4.15	123.5	0.30

The total installed heat pump capacity is $7.8\,kW_{th}$, which exceeds the peak cooling demand of the building in both locations ($4.0\,kW_{th}$ for Madrid and $3.7\,kW_{th}$ for Rome), calculated using the ASHRAE method [25]. The electric consumption of the heat pumps is estimated assuming an operating load of 70 % of the maximum capacity and a seasonal energy efficiency ratio (SEER) of 3.5. The indoor air temperature setpoint was fixed at 23 °C (and adopted also for peak cooling demand calculation). Table S19 presents the resulting heat pump energy consumption and design characteristics. As expected, the thermal energy removed by the heat pump differs from that removed by the RCMs because the heat pump maintains indoor air temperature within a narrow range around the setpoint (±0.5 °C).

The capital cost difference between the novel DRC-based system and the conventional heat pumps is calculated as:

$$\Delta CapEx = C_{HP} - (C_{SR} + C_{RCM} + C_{ds}) - C_{inc} \tag{S39}$$

where:

- $C_{HP} = \bar{C}_{HP}\, n_{HP}$ is the total cost of heat pumps where $\bar{C}_{HP}$: cost of heat pump per unit ($EUR\,unit^{-1}$), $n_{HP} = 3$: number of units;

Table S18: DRC-based cooling system performance in Madrid and Rome

Parameter	Symbol	Madrid	Rome
Thermal energy removed ($kWh_{th}\ yr^{-1}$)	E_{RCM}	3651	3038
Comfort index (%)	CI	99%	99%
DRC system SEER (-)	SEER	189	150
DRC system el. energy consumption ($kWh_{el}\ yr^{-1}$)	$E_{el,pump}$	19.3	20.3

Table S19: Heat pump performance in Madrid and Rome

Parameter	Symbol	Madrid	Rome
Heat pump SEER in cooling mode (-)	$SEER_{HP}$	3.2 / 5.4	3.2 / 5.4
Heat pump el. energy consumption ($kWh_{el}\ yr^{-1}$)	$E_{el,HP}$	996	795
Evaporator nominal capacity (kW_{th})		2.6	2.6
Condenser nominal capacity (kW_{el})		3.4	3.4
Compressor nominal capacity (kW_{th})		0.75	0.75
Refrigerant flow rate ($kg\ s^{-1}$)		0.0196	0.0196

Table S20: Economic and environmental parameters for Madrid and Rome

Parameter	Symbol	Madrid	Rome	Ref.
SRs investment cost ($EUR\ m^{-2}$)	$\bar{C}_{SR}$	65 / 40	65 / 40	[26] / estimated
RCMs investment cost ($EUR\ unit^{-1}$)	$\bar{C}_{RCM}$	51.2	51.2	estimated
Heat pump investment cost ($EUR\ unit^{-1}$)	$\bar{C}_{HP}$	350 / 500	350 / 500	market data
Electricity retail price ($EUR\ kWh_{el}^{-1}$)	$\bar{C}_{el}$	0.261	0.329	[27]
Green grants (% of investment cost)		0 % / 20 %	0 % / 20 %	assumed
Grid emission factor ($kg_{CO_2}\ kWh_{el}^{-1}$)	f_{el,CO_2}	0.129	0.180	[28]

- $C_{SR} = \bar{C}_{SR}\ A_{SR}$ is the total cost of SRs where $\bar{C}_{SR}$: cost of SRs per unit surface ($EUR\ m^{-2}$), $A_{SR} = 65.8\ m^2$: total SR surface;
- $C_{RCM} = \bar{C}_{RCM}\ n_{RCM}$ is the total cost of RCMs where $\bar{C}_{RCM}$: cost of RCMs per unit ($EUR\ unit^{-1}$), $n_{RCM} = 70$: number of units;
- C_{ds} is the cost of the DRC-system water distribution subsystem (piping, collectors, circulation pump, buffer tank, and safety devices), assumed to be 10 % of the combined cost of SRs and RCMs.
- C_{inc} is the cost reduction associated with eligibility for green grants or incentive schemes (assumed to be applied as a percentage reduction of the capital cost).

This capital cost difference represents a simplified estimate because it excludes installation costs for both the heat pumps and the DRC-based system, a cost component that significantly affects both technologies. Installation costs account for labor required to assemble and commission the cooling system and depend strongly on geographical location.

The operational cost difference between the novel DRC-based system and the conventional heat pump system is:

$$\Delta OpEx = \bar{C}_{el,HP}\left(E_{el,HP} - E_{el,pump}\right) \tag{S40}$$

where $\bar{C}_{el}$ is the retail price of electricity (including taxes and levies) for household consumption ($EUR\ kWh_{el}^{-1}$), $E_{el,HP}$ is the seasonal electric consumption of the heat pumps for cooling and $E_{el,pump}$ is the seasonal electricity consumption of the circulation pump in the DRC-based system. The operational cost difference neglects the routine maintenance costs of both systems.

The CO_2 emissions avoided by the DRC-based cooling systems relative to the conventional heat pumps during the cooling season are calculated as:

$$\Delta CO_2 = f_{el,CO_2}\left(E_{el,HP} - E_{el,pump}\right) \tag{S41}$$

where f_{el,CO_2} denotes the national electric grid emission factor ($kg_{CO_2}\ kWh_{el}^{-1}$). Table S20 lists the parameters adopted throughout the economic analysis together with their corresponding references.

The economic analysis was carried out under two different scenarios:

- Favorable scenario: the novel DRC system is compared with a low-efficiency heat pump (SEER = 3.2, $\bar{C}_{HP} = 350\ EUR\ unit^{-1}$). The investment is eligible for green grants (−20 % on the investment cost), and the cost of SRs is assumed to be lower than current values ($\bar{C}_{SR} = 40\ EUR\ m^{-2}$).
- Neutral scenario: the novel DRC system is compared with a high-efficiency heat pump (SEER = 5.4, $\bar{C}_{HP} = 500\ EUR\ unit^{-1}$). The investment is not eligible for green grants, and the cost of SRs is assumed to match current values ($\bar{C}_{SR} = 65\ EUR\ m^{-2}$).

Table S21 reports the results of the economic and environmental analysis for Madrid and Rome during the cooling season under both scenarios.

Table S21: Economic and environmental analysis results for different scenarios

Scenarios	Favorable, Madrid	Favorable, Rome	Neutral, Madrid	Neutral, Rome
DRC system investment cost (EUR)	5470	5470	8650	8650
Heat pump investment cost (EUR)	1050	1050	1500	1500
DRC-based system operational cost (EUR yr^{-1})	5.0	6.7	5.0	6.7
Heat pump operational cost (EUR yr^{-1})	284.0	286.0	168.3	169.5
ΔCapEx (EUR)	-4420	-4420	-7150	-7150
ΔOpEx (EUR yr^{-1})	279.0	279.3	163.3	162.8
ΔCO_2 (kg_{CO_2} yr^{-1})	138	153	81	89

Supplementary Figures

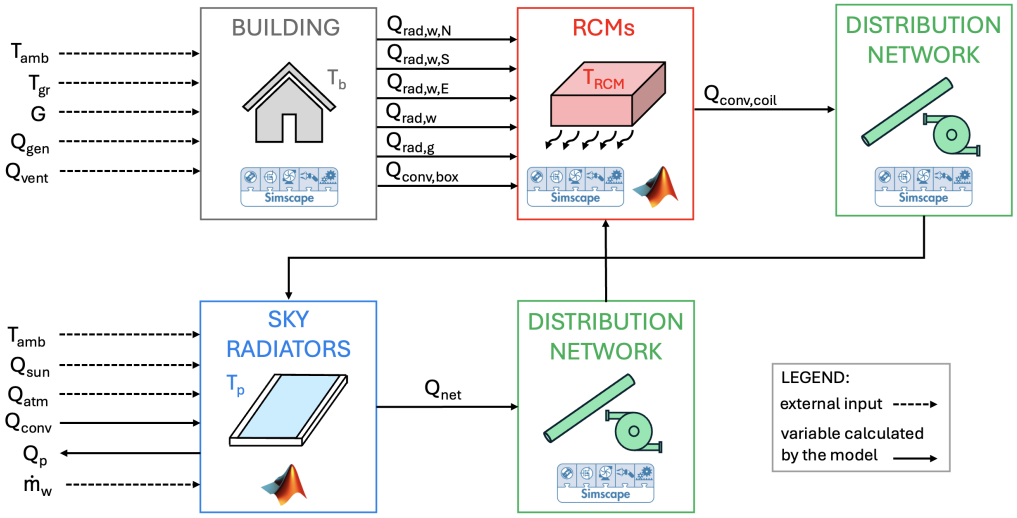

Figure S1. Schematic of the transient model, illustrating the subsystems implemented in Matlab and Simscape environments, along with the corresponding inputs and outputs for each subsystem.

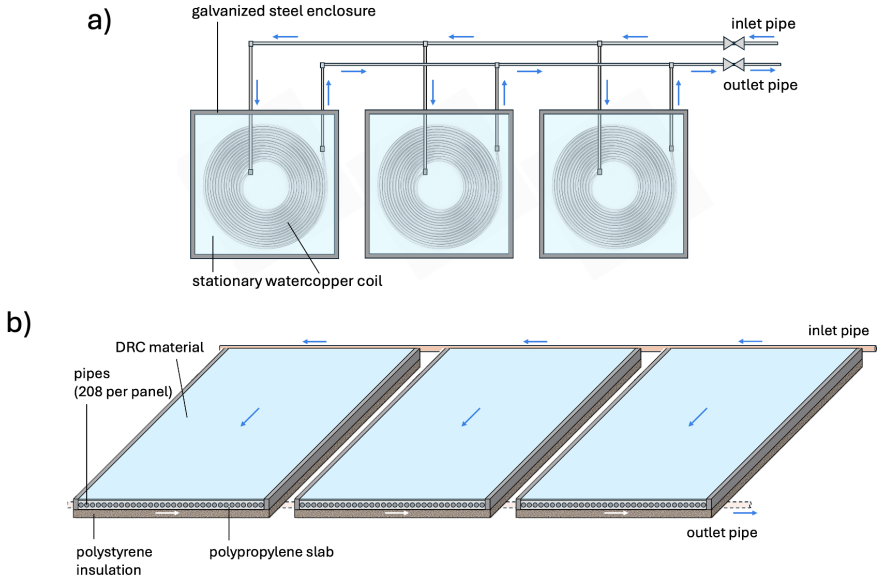

Figure S2. a) Schematic of the Radiative Cooling Modules (RCMs). b) Schematic of the Sky Radiators (SRs). Schematics are not drawn to scale.

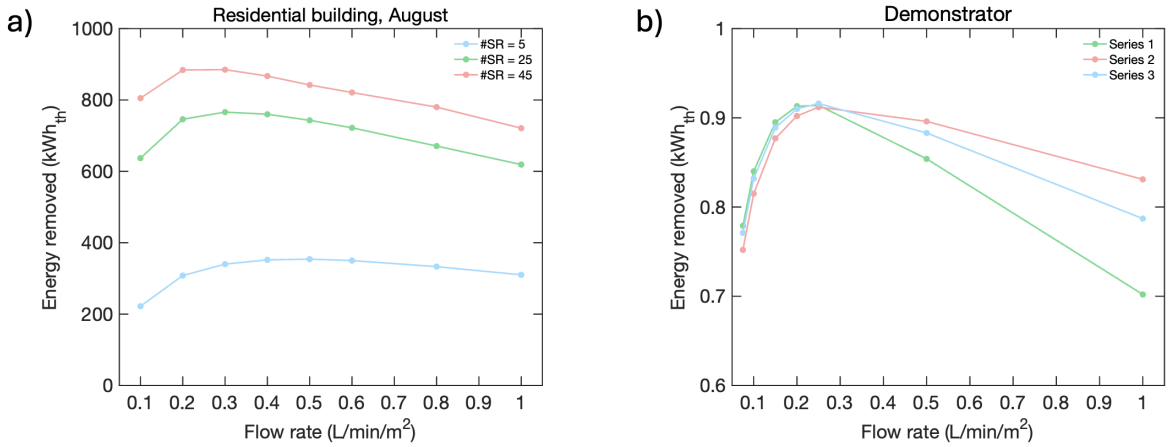

Figure S3. Effect of water flow rate on the energy removed by RCMs. a) Results for the large single-family building using August TMY data, with 60 RCMs, 12 pumping hours, a commercial DRC emitter, and varying numbers of SRs (5, 25, 45). b) Extrapolations on the demonstrator under three meteorological series: Series 1 (20/08–24/08/2024), Series 2 (8/08–12/08/2024), and Series 3 (16/08–20/08/2024), with 8 RCMs, 5 SRs, 12 pumping hours (9:00 PM – 9:00 AM) and a commercial DRC emitter.

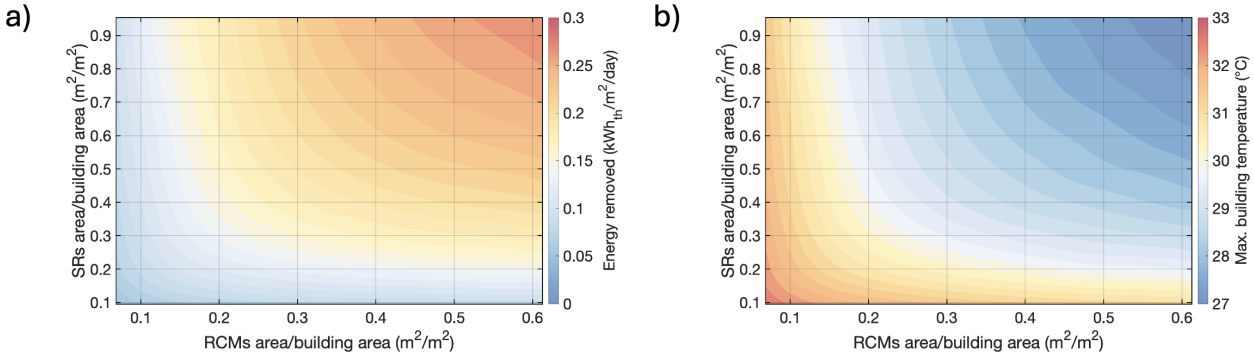

Figure S4. SR and RCM sizing analysis for a single-family building in Madrid during August (TMY), with commercial DRC material and a water flow rate of 0.25 L/min/m^2. a) Thermal energy removed by the RCM per m^2 of building surface. b) Maximum indoor building temperature.

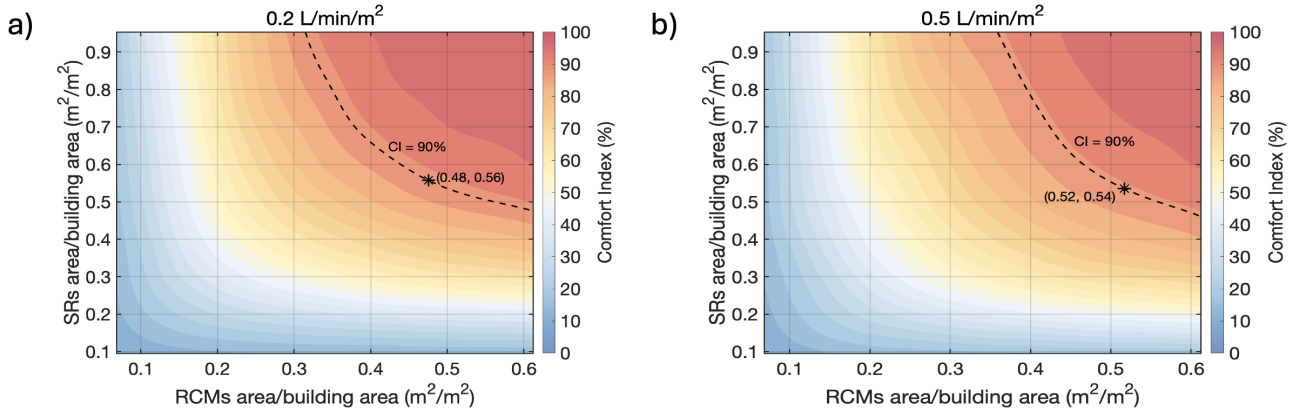

Figure S5. SR and RCM sizing analysis for a single-family building in Madrid during August (TMY), with commercial DRC material. Comfort index for a water flow rate of a) 0.2 L/min/m^2; b) 0.5 L/min/m^2.

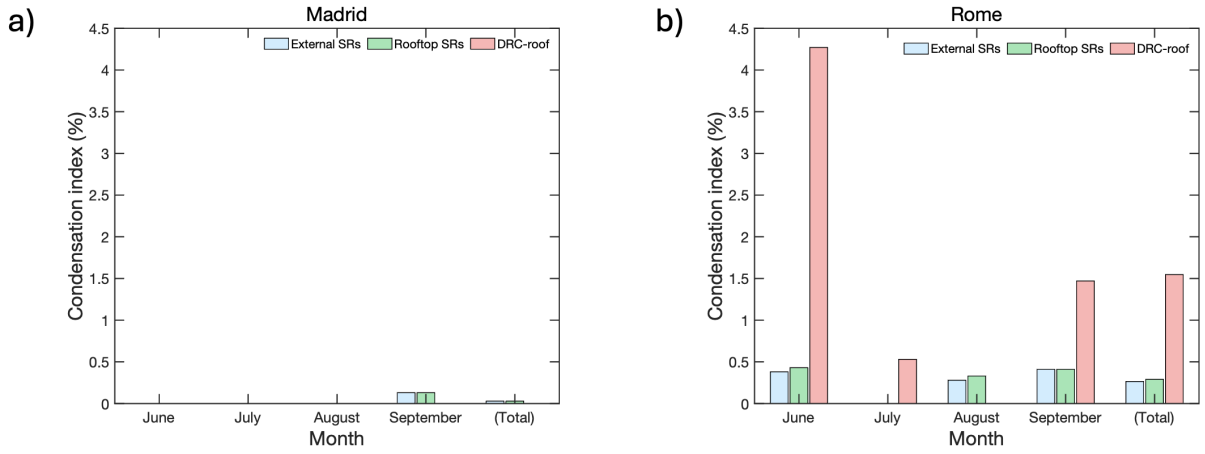

Figure S6. Condensation risk analysis for a single-family building in Madrid during August (TMY), using commercial DRC material, a flow rate of 0.25 L/min/m^2 and 70 RCMs. Three scenarios are evaluated: 29 external SRs (blue bars), 29 rooftop SRs (green bars), and a passive DRC-roof configuration (red bars).

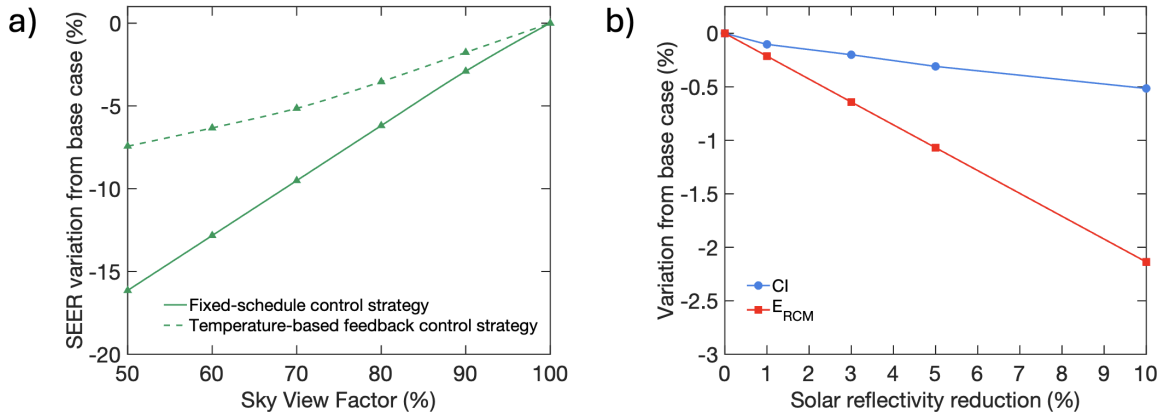

Figure S7. a) Effect of sky view factor on comfort index, energy removed by RCMs and SEER compared to the base case (SVF=100%). b) Effect of DRC material solar reflectivity reduction on comfort index and energy removed by RCMs compared to base case (unaged DRC material). Both analyses refer to a single-family building in Madrid during August (TMY), using commercial DRC material, a flow rate of 0.25 L/min/m^2, 29 external SRs, 70 RCMs and the optimal number of pumping hours (13 hours for August).

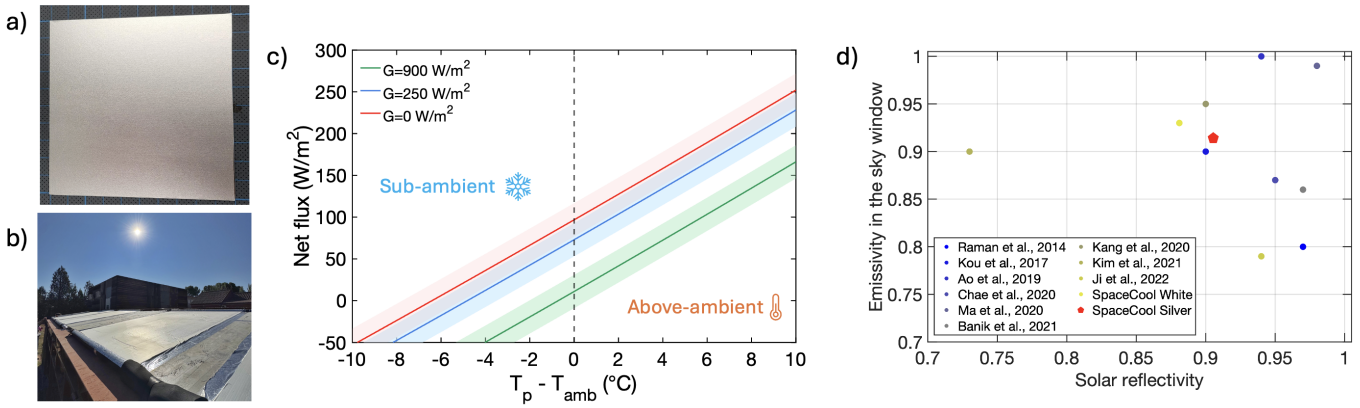

Figure S8. a) Sample of the SpaceCool_silver DRC material. b) SpaceCool_silver film on the SRs in the Arganda del Rey full-scale demonstrator. c) Thermal characteristic of the SpaceCool_silver material (net flux vs. subcooling relative to ambient) under three different solar irradiance levels; shaded areas indicate the variation range for relative humidity between 20% and 80%. d) Comparison of the optical properties of SpaceCool_silver with other DRC materials reported in the literature (data sourced from Ref. [29]).

References

[1] Tobias Loga, Britta Stein, and Nikolaus Diefenbach. Tabula building typologies in 20 european countries—making energy-related features of residential building stocks comparable. *Energy and Buildings*, 132:4–12, 2016.

[2] Alejandra García-Prieto Ruiz, Begoña Serrano Lanzarote, and Leticia Ortega Madrigal. Catálogo de tipología edificatoria residencial. *Ámbito: España*, 2016.

[3] Vincenzo Corrado, Ilaria Ballarini, Stefano Paolo Corgnati, and Novella Talà. Building typology brochure–italy. *Fascicolo sulla Tipologia Edilizia Italiana*, pages 1–117, 2011.

[4] I Jankovic, X Fernandez, and J Diriken. Database of grey-box model parameter values for EU building typologies. *Ambience EU Project Report*, 2021.

[5] Código Técnico de la Edificación. Ministerio de la vivienda. *Real Decreto*, 314, 2006.

[6] Alessandro Prada, Marco Baratieri, Paolo Baggio, Piercarlo Romagnoni, Andrea Gasparella, et al. Caratteristiche dinamiche dei componenti edilizi: metodi semplificati (uni en iso 13786), modellazione dettagliata e dati sperimentali. In *Certificazione energetica: normative e modelli di calcolo per il sistema edificio-impianto posti a confronto*, pages 371–382. AICARR, 2008.

[7] Meysam Mahooti. NREL's Solar Position Algorithm (SPA), 2025. `https://www.mathworks.com/matlabcentral/fileexchange/59903-nrel-s-solar-position-algorithm-spa` Last accessed: 14/06/2025.

[8] Steven Vajk Szokolay. Solar geometry. In *PLEA: Passive and Low Energy Architecture. PLEA note 1*. PLEA, 1996.

[9] Frank P Incropera, David P DeWitt, Theodore L Bergman, Adrienne S Lavine, et al. *Fundamentals of heat and mass transfer*, volume 6. Wiley New York, 1996.

[10] Isidoro Martinez. Radiative view factors. 2013.

[11] Davide Forte, Claudio Belotti, Lorenzo Pattelli, Matteo Morciano, Eliodoro Chiavazzo, Pietro Asinari, and Matteo Fasano. Modeling of daytime radiative cooling enhanced vapor-compression refrigeration systems. *Energy*, 340:139101, 2025.

[12] Prabhata K Swamee and Akalank K Jain. Explicit equations for pipe-flow problems. *Journal of the hydraulics division*, 102(5):657–664, 1976.

[13] CM White. Streamline flow through curved pipes. *Proceedings of the Royal Society of London. Series A, Containing Papers of a Mathematical and Physical Character*, 123(792):645–663, 1929.

[14] H Itō and K Imai. Energy losses at 90 pipe junctions. *Journal of the Hydraulics Division*, 99(9):1353–1368, 1973.

[15] E. González-Cruz, G. Pérez, F. Borja, C. Alonso, F. Martin-Consuegra, E. Krüger, A. Gutierrez, and B. Arranz. Full-scale facility for the assessment of night and daytime passive radiative cooling. In *Proceedings of 2024 CATE Conference, 20-22 November 2024 Seville, Spain*, page 179, November 2024.

[16] AK Das and M Iqbal. A simplified technique to compute spectral atmospheric radiation. *Solar Energy*, 39(2):143–155, 1987.

[17] AJ Prata. A new long-wave formula for estimating downward clear-sky radiation at the surface. *Quarterly Journal of the Royal Meteorological Society*, 122(533):1127–1151, 1996.

[18] ASHRAE. *ANSI/ASHRAE Standard 55-2017: Thermal Environmental Conditions for Human Occupancy*. ASHRAE, Atlanta, 2017.

[19] M Dirksen, RJ Ronda, NE Theeuwes, and GA Pagani. Sky view factor calculations and its application in urban heat island studies. *Urban climate*, 30:100498, 2019.

[20] Haida Tang, Xingkang Chai, Wang Jing, Yemao Li, and Chunying Li. Assessment of photovoltaic power generation and radiative cooling potentials in old residential districts: A case study of shenzhen. *Energy and Buildings*, 319:114493, 2024.

[21] A Adibekyan, J Schumacher, Lorenzo Pattelli, Jochen Manara, S Meriç, Ö Bazkir, Carlo Cucchi, C Sprengard, G Pérez, J Campos, et al. Emissivity and reflectivity measurements for passive radiative cooling technologies. *International Journal of Thermophysics*, 46(5):1–16, 2025.

[22] DG Erbs, SA Klein, and JA Duffie. Estimation of the diffuse radiation fraction for hourly, daily and monthly-average global radiation. *Solar energy*, 28(4):293–302, 1982.

[23] Jianing Song, Qingchen Shen, Huijuan Shao, and Xu Deng. Anti-environmental aging passive daytime radiative cooling. *Advanced Science*, 11(10):2305664, 2024.

[24] Yue He, Biao Lu, Jinzhong Fang, Yue Lei, Shan Gao, and Chi Feng. Radiative cooling for long-term building energy efficiency: an experimental comparison of seven coatings. *National Science Open*, 3(3):20230065, 2024.

[25] *2021 ASHRAE Handbook, Fundamentals*. American Society of Heating, Refrigerating and Air-Conditioning Engineers, 2021.

[26] Vinay Kumar Yadav, Kumar Gautam, Jahar Sarkar, and Pradyumna Ghosh. Techno-economic assessment of novel solar-driven dual-mode trigeneration device featuring daytime radiative condenser. *Energy*, page 137116, 2025.

[27] Eurostat. Electricity prices for household consumers. `https://doi.org/10.2908/NRG_PC_204`. Accessed: 24 November 2025.

[28] European Environment Agency (EEA). Greenhouse gas emission intensity of electricity generation in europe. `https://www.eea.europa.eu/en/analysis/indicators/greenhouse-gas-emission-intensity-of-1`. Accessed: 24 November 2025.

[29] Ioannis Kousis and Anna Laura Pisello. Toward the scaling up of daytime radiative coolers: A review. *Advanced Optical Materials*, 11(21):2300123, 2023.